Flexible and Printed Electronics

PAPER

Understanding resistance increase in composite inks under monotonic and cyclic stretching

To cite this article: Q Li *et al* 2022 *Flex. Print. Electron.* **7** 045010

Flexible and Printed Electronics

CrossMark

RECEIVED
27 September 2022

REVISED
30 November 2022

ACCEPTED FOR PUBLICATION
7 December 2022

PUBLISHED
21 December 2022

PAPER

Understanding resistance increase in composite inks under monotonic and cyclic stretching

Q Li, A Antoniou* **and O Pierron***

G.W. Woodruff School of Mechanical Engineering, Georgia Institute of Technology, Atlanta, GA 30318, United States of America

* Authors to whom any correspondence should be addressed.

E-mail: antonia.antoniou@me.gatech.edu and olivier.pierron@me.gatech.edu

Keywords: conductive inks, cyclic stretching, failure lifetime, geometrical effects

Supplementary material for this article is available online

Abstract

Cyclic degradation in flexible electronic inks remains a key challenge while their deployment in life critical applications is ongoing. The origin of electrical degradation of a screen-printed stretchable conductive ink with silver flakes embedded in a polyurethane binder is investigated under uniaxial monotonic and cyclic stretching, using *in-situ* confocal microscopy and scanning electron microscopy experiments, for varying ink thickness (1, 2, and 3 layers, each layer around 8–10 μm) and trace width (0.5, 1, and 2 mm). Cracks form under monotonic stretching, and the evolution of crack pattern (density, length and width) with applied strain is affected by ink thickness such that the 3-layer ink exhibits larger normalized resistance but slightly lower resistance than the 1-layer ink up to strains of 125%. For cyclic stretching, the crack density and length do not evolve with cycling. However, the cracks widen and deepen, leading to an increase in resistance with cycling. There exists a strong correlation between fatigue life, i.e. the number of cycles until a normalized resistance of 100 is reached, and the strain amplitude. The normalized resistance increase rate with respect to cycling is also found to scale with strain amplitude. The rate of change in resistance with cycling decreases with ink thickness and trace width. For practical applications, thicker ($\geqslant$25 μm) and wider ($\geqslant$2 mm) inks should be used to lower resistance increases with repeated deformation.

1. Introduction

Flexible electronic devices have gained broad interest for their applications in wearable healthcare monitoring [1–6], energy storage [7–10], flexible displays [11–17], and implantable bioelectronics [18, 19], to name a few. These devices can integrate rigid or even soft electronic components with compliant, conformable electric circuits based on stretchable and flexible conductive interconnects. A major challenge for these flexible devices is maintaining the electrical performance of the conductive interconnects after repeated deformation, such as repeated elongation. In wearable devices, this loading results in strains of up to 30%–50% [20, 21].

A significant amount of research effort has been made to understand and improve the electrical reliability of the conductive interconnects. One approach to improving electrical reliability is by changing the material composition of the interconnect. Thin metal film interconnects deposited on polymer substrates offer initially high electrical conductivity, but their usage is limited by the substantial elastic mismatch between the thin metal film and the polymer substrate, which leads to the loss of conductivity at low strains (typically ~10%) due to cracking [22–30] and metal fatigue [31–33]. Another class of interconnects are composite conductive inks consisting of conductive metal flakes embedded in an elastomer binder [34–43]. These conductive inks have shown promise as electrical interconnects due to their tolerance of higher applied strains when mounted on polymer substrates. The current work studied the PE874 conductive ink provided by DuPont, which is a stretchable ink with silver flakes embedded in a polyurethane binder. The PE874 ink is screen printed onto the TE-11 C thermoplastic polyurethane (TPU) substrate.

A second approach to improving the electrical reliability of the interconnects involves optimizing the structural configuration of the interconnect lines by changing their sizes, shapes, and structures. Numerous works [44, 45] have shown that serpentine shaped interconnects could greatly improve electrical performance under tensile strain compared to straight trace lines and can tolerate cyclic loading, due to the maximum local strain being more than an order of magnitude lower than the macroscale applied strains [44, 46]. To characterize the electrical resistance evolution of a conductive ink with both monotonic and cyclic uniaxial elongation for a wide range of strain, specimens with straight trace lines were studied in a number of prior works by Cahn *et al* [34, 47, 48] due to the relatively uniform deformation and ease of achieving high strains experimentally. The conductive ink's electrical resistance evolution with monotonic or cyclic strain, obtained from tests using the straight trace line specimens, can potentially be used to map and predict the resistance evolution in more complex configurations such as serpentines. The width of the interconnect line (trace width) was shown by Sliz *et al* [45] to be an important factor in determining the electrical performance of serpentine configured conductive inks; ink thickness could be another important factor. These geometric effects can be investigated efficiently using straight trace line specimen due to the relatively uniform strain distribution.

The current work provides a comprehensive investigation of the effects of critical ink geometry and loading conditions on the electrical response of the PE874 ink under uniaxial monotonic and cyclic stretching, as well as a better understanding of the underlying mechanisms behind the electrical resistance increase, thanks to *in-situ* confocal microscope and *in-situ* scanning electron microscopy (SEM) experiments. The effects of the lengthening, widening, and deepening of the cracks on the electrical resistance evolution with monotonic strain were examined. A series of cyclic stretching (fatigue) tests were performed to investigate the effects of cycling conditions, including the strain amplitude and mean strain during cycling, and geometric conditions, including the ink thickness and trace width, on resistance evolution.

2. Experimental procedures

2.1. Ink deposition and characterization

The PE874 conductive ink formulated by DuPont is composed of silver flakes embedded in a polyurethane binder material. The average volume fraction of silver flakes in the ink is about 55% [34]. The PE874 ink test specimens consist of 1, 2, or 3 layers of the PE874 ink screen printed onto a TPU substrate layer in a single pass (for 1-layer specimens) or multiple passes (for 2- and 3-layer specimens). The TPU used for the substrate is the TE-11 C from DuPont. The screen-printing process was performed at the DuPont Applications Laboratory with proprietary processes that have been optimized for the ink and substrate. For the first ink layer, a mesh size of 325 threads crossing per inch^2 with wire diameter of 0.9 mil was used. For the second and third ink layer, a mesh size of 280 threads crossing per inch^2 with wire diameter of 1.2 mil was used. For all cases, mesh angle was 30°. There was a 15 min drying time after the printing of each ink layer, at 125 °C for the first ink layer and 130 °C for the subsequent layers. The silver flakes had sizes ranging from several μm to 100s of nm, and occupied 55% of the total volume on average. In addition, there was a large amount of voids in the ink microstructure, with sizes also ranging from several μm to 100s of nm and occupying 17% of the total volume on average. The ink is printed in U-shaped, double trace lines with 2 mm, 1 mm, or 0.5 mm trace width (see figure 1(a)). The four pads in the print pattern were designed for four-point electrical resistance probes. The average thicknesses of the 1, 2, and 3 ink layers measured by DuPont are 10 μm, 20 μm, and 25 μm, respectively. FIB cross-section images of the 1-layer and 3-layer ink are shown in figures 1(b) and (c), respectively. The average thickness of the TPU substrate is 127 μm.

2.2. Monotonic experiments

The monotonic tension experiments were performed on a number of 1, 2, and 3-layered specimens with 2 mm and 0.5 mm trace widths to obtain the electrical resistance response to tensile strain. The monotonic tension experiments were performed using the Linkam scientific TST350 microtensile test stage at a strain rate of 2% per second, while the electrical resistance is measured using the Agilent 34 401 A digital multimeter (see figure 1(d)). The resistance is reported as the normalized value R/R_0, where R is the resistance at strain ε and R_0 is the initial resistance before deformation. Due to the distance d_{clamp} between the specimen clamps (about 30 mm) being shorter than half the overall length l_{print} of the double trace line (38 mm), the initial resistance R_0 needed to be adjusted for the unstrained portion of the specimen:

$$R_0 = R_{\text{measured},\varepsilon=0} \times \left(\frac{d_{\text{clamp}}}{l_{\text{print}}/2}\right). \quad (1)$$

The resistance R is the sum of the initial resistance R_0 and the measured change in resistance ΔR, which is entirely attributed to the strained portion of the specimen.

$$\Delta R = R_{\text{measured},\varepsilon} - R_{\text{measured},\varepsilon=0} \quad (2)$$

$$R = R_0 + \Delta R. \quad (3)$$

The initial resistance R_0 for the 1-, 2-, and 3-layer inks with 0.5 and 2 mm width, are plotted in figure 1(e).

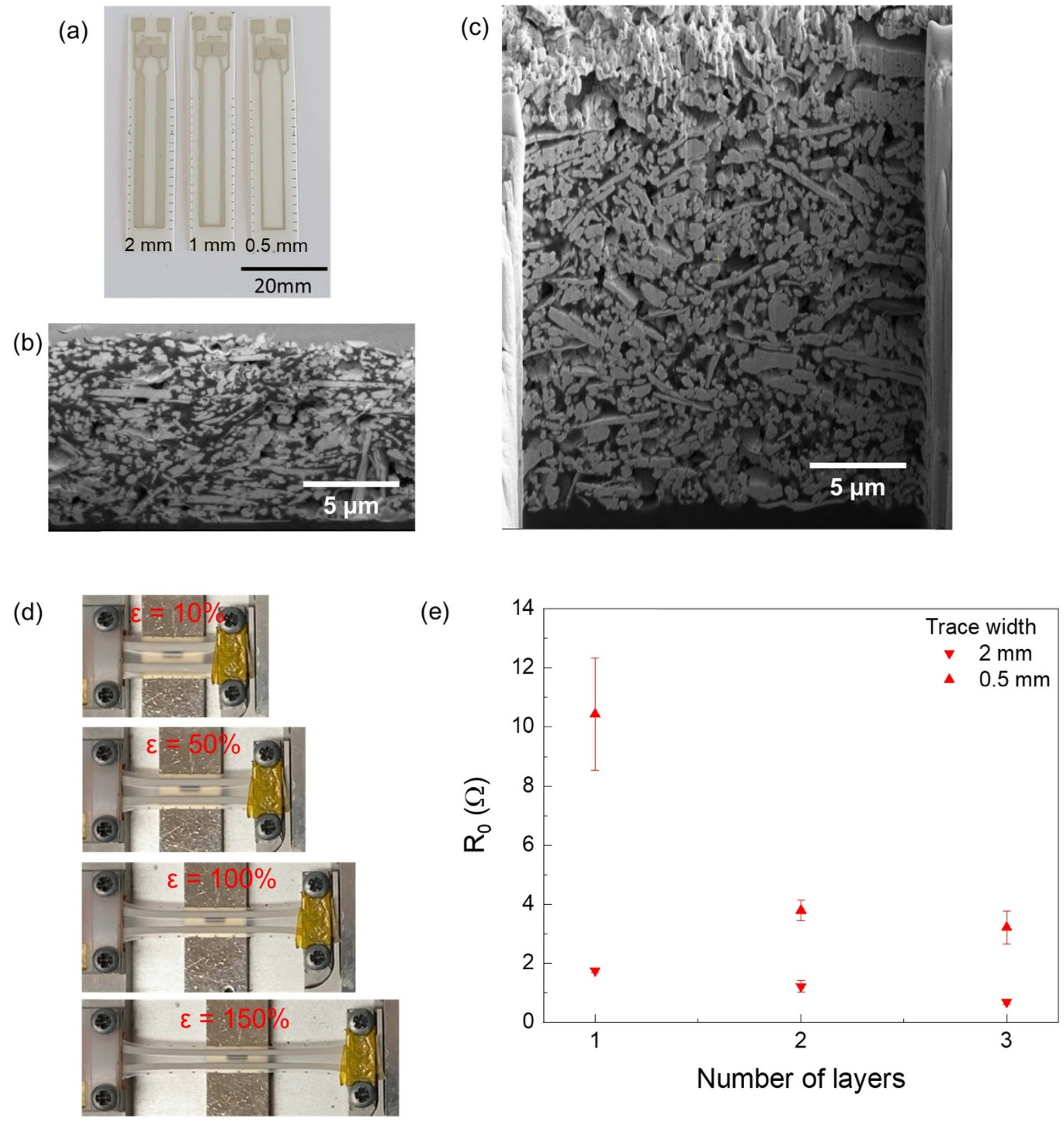

Figure 1. (a) Specimens with 2 mm, 1 mm, and 0.5 mm trace widths (left to right); FIB cross-sections for (b) 1-layer and (c) 3-layer ink; (d) specimen under different tensile strains in the Linkam TST350 testing stage; (e) R_0 for specimens with different number of layers and trace widths in monotonic tests.

2.3. Fatigue experiments

The fatigue (cyclic tensile stretching) experiments were performed using the same setup as the monotonic tension experiments. In a fatigue experiment, a cyclic loading scheme was implemented with a mean strain of ε_m and strain amplitude of ε_a. The specimen was first elongated to a maximum strain of $\varepsilon_m + \varepsilon_a$, then strain cycled between the minimum strain $\varepsilon_m - \varepsilon_a$ and maximum strain $\varepsilon_m + \varepsilon_a$. A strain rate of 2% per second was also used for the fatigue experiments.

The ink electrical resistance, R, cycles between a maximum and minimum during every loading cycle, and the maximum R during a stretching cycle increases with cycling. The rate of change in R/R_0 with respect to cycles, or $(R/R_0)'$, at cycle N was calculated by fitting a linear regression function to the R/R_0 maxima for a set of cycles between $N-4$ and $N+4$, excluding any null points at the beginning or end of the set of cycles. The choice of using the cycles $N-4$ to $N+4$ for the linear regression fitting was made by trial to achieve the generally smooth evolution of $(R/R_0)'$ over the cycles.

2.4. *In situ* experiments

In-situ monotonic tension and fatigue experiments were also performed under an Olympus LEXT 4100 confocal microscope. The monotonic experiments were paused at intervals of strain and the fatigue experiments were paused at intervals of cycles in order to capture *in-situ* optical images and laser profilometry scans of the ink surface at the maximum strain during the cycle. The optical images provided measurements of the length and density of the cracks on the ink surface. The laser profilometry scans characterized the ink surface topography and therefore the crack width. Both the optical images and laser profilometry scans were taken at a resolution of 0.62 μm/pixel and had approximate dimensions of 639 $\times$ 639 μm. *In-situ* monotonic tension experiments were performed with 3-layer 2 mm, 1-layer 2 mm, 3-layer 0.5 mm, and 1-layer 0.5 mm specimens to examine the effect of ink thickness and trace width on the crack pattern in the ink under tensile strain. *In-situ* fatigue experiments were performed with 3-layer 2 mm, 1-layer 2 mm, and 3-layer 0.5 mm specimens to examine the effect of cyclic loading on crack width.

A separate *in-situ* experiment was performed inside the Thermo Helios 5 CX focused ion beam-scanning electron microscope (FIB-SEM). The experiment consisted of a monotonic tension experiment on a 3-layer 1 mm specimen paused at intervals of strain to capture *in-situ* SEM images of the ink surface. This is followed directly by a fatigue (cyclic tensile stretching) experiment on the same specimen paused at different cycles to capture *in-situ* SEM images of the ink surface. The *in-situ* SEM experiment was performed on a Kammrath & Weiss MZ0-1 tension/compression testing module (narrow version). The distance between the grips was 15 mm and both the monotonic and fatigue experiments were performed at a strain rate of 0.133% per second. In-plane strain maps from the SEM *in-situ* images were obtained using the digital image correlation (DIC) Ncorr software [49]. In addition, an *ex-situ* fatigue experiment was performed using the Linkam testing stage at a strain rate of 0.2% per second to obtain the expected R/R_0 evolution data.

3. Results and discussion

3.1. Monotonic behavior

Figure 2(a) shows the effect of number of layers on the normalized resistance (R/R_0)—applied strain (ε) data for the monotonic tensile stretching experiments (up to 150% strain) with 2 mm-wide specimens, while figure 2(b) highlights the effect of specimen width for the 3-layer specimens. The initial R_0 values for the different specimen configurations are also plotted in figure 1(e). For a given strain, the normalized resistance increases with number of layers (see figure 2, when accounting for the thickness effect on R_0 (figure 1(e)), the results indicate that, at a given strain, the resistance slightly decreases with increasing number of layers. This is clearly shown in figure 2(c) where the ratio of normalized resistance, R/R_0, is plotted, for both 2 vs 1 layer and 3 vs 1 layer. Comparing 3 layers vs 1 layer, the ratio of normalized resistance is always less than 2.5, while the ratio of initial resistance (1 layer vs 3 layers) is 2.55 (as expected based on the measured thicknesses of 10 μm for 1 layer and 25 μm for 3 layers; see figures 1(b) and (c)). Hence these results demonstrate that using thicker inks decreases the overall resistance even at large strains.

The R/R_0 of the 3-layer 0.5 mm-wide specimens increased much more quickly with ε than the 2 mm-wide specimens (see figure 2(b)). Therefore, the trace width effect found by Cahn *et al* [48] in the 1-layer ink can be extended to multi-layer inks. In other words, the width should be 2 mm or more to minimize both normalized resistance and resistance (since wider traces have lower R_0) with strain.

The ink thickness and trace width effects can be understood by the observation of the crack pattern in the *in-situ* monotonic stretching experiments. From the confocal optical images for the 1-layer and 3-layer 2 mm-wide specimens (figure 2(a)), the lengths and area density of the cracks in the specimens with different ink thicknesses could be analyzed. The surface cracks in these two specimens at 10% strain, identified by visual inspection, are highlighted in figures 3(a) and (b). The lengths of the cracks are sorted in the histograms of figures 3(c) and (d). The mean crack length was 347 μm for the 3-layer and 102 μm for the 1-layer 2 specimen. For the 3-layer specimen, a significant number of cracks had lengths exceeding 0.5 mm; for the 1-layer specimen, none of the cracks exceeded a length of 0.3 mm. The area density of the cracks in a specimen was calculated by dividing the total crack count by the observed area. The area crack density was about 27 cracks per mm^2 for the 3-layer and 95 cracks per mm^2 for the 1-layer specimen at 10% strain. Therefore, the 1-layer specimen had a network of more numerous, shorter cracks while the 3-layer specimen had a network of fewer, longer cracks. The relation between thicker ink and greater crack spacing is also found in thin metal films supported by polymer substrates [50–52]. The greater lengths of the cracks in the 3-layer specimen, some of which exceeded 0.5 mm (figure 3), enabled the traversal of the entire 0.5 mm trace width by some of the cracks in the 3-layer 0.5 mm-wide specimen (figure 2(b)). At higher strains (>50%), the cracks in the 3-layer ink traversing the 0.5 mm trace line were observed to widen drastically, leading to a rapid increase in R/R_0.

Figure 4 shows SEM images of the crack pattern from the monotonic part of the *in-situ* SEM experiments with the 3-layer and 1-layer 1 mm-wide specimens and the $R/R_0-\varepsilon$ data from the corresponding *ex-situ* experiments. Similar to the optical images for the 2 mm-wide specimens in figure 1, the low magnification SEM images in figure 4(a) also highlight a clear distinction between the longer cracks in the 3-layer ink and the shorter cracks in the 1-layer ink. At 30% strain, cracks coalescence traversing more than 50% of the trace line had already occurred at several locations within the imaged area for the 3-layer specimen, while the shorter and more numerous cracks in the 1-layer specimen could not coalesce into such

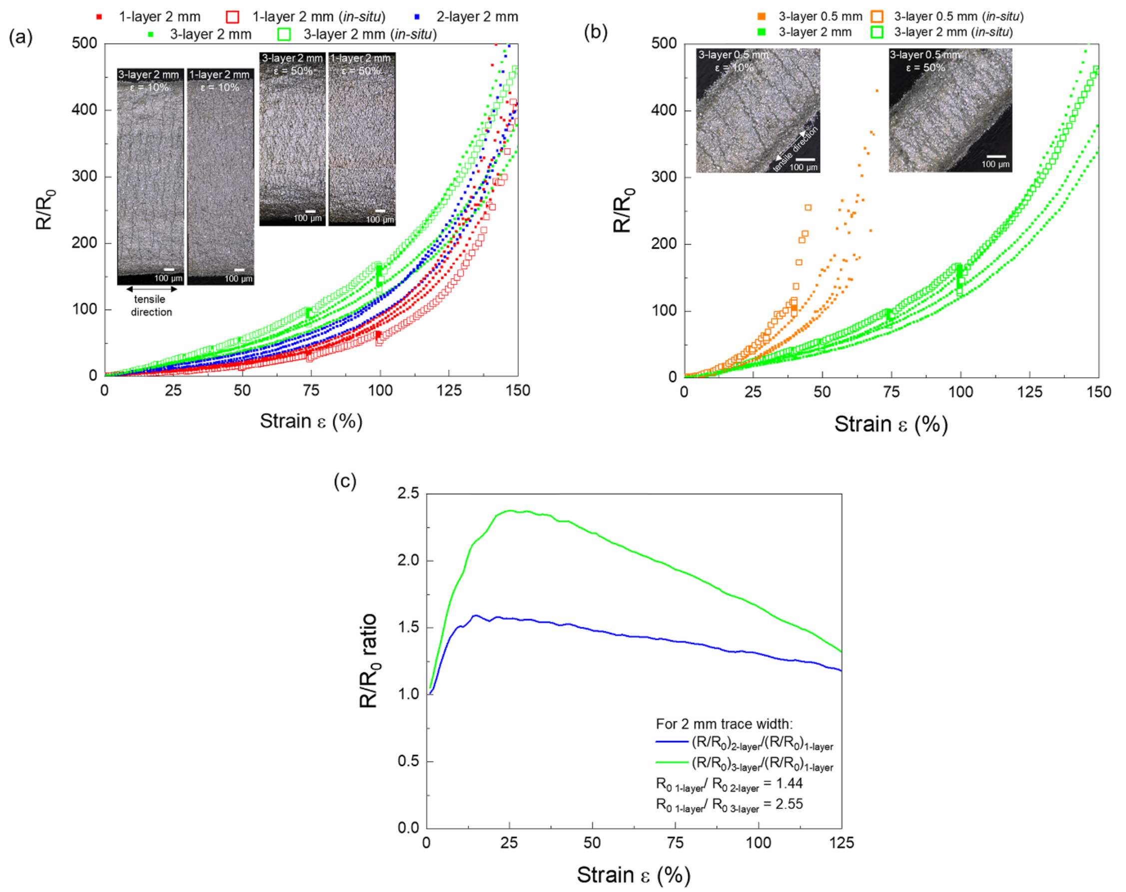

Figure 2. $R/R_0 - \varepsilon$ evolution from monotonic stretching tests and crack pattern images from *in-situ* confocal microscope monotonic stretching tests for (a) 2 mm specimens with 1, 2, and 3 ink layers and (b) 3-layer specimens with 0.5 mm and 2 mm trace widths; (c) R_0 for specimens of different layers and trace widths in monotonic tests.

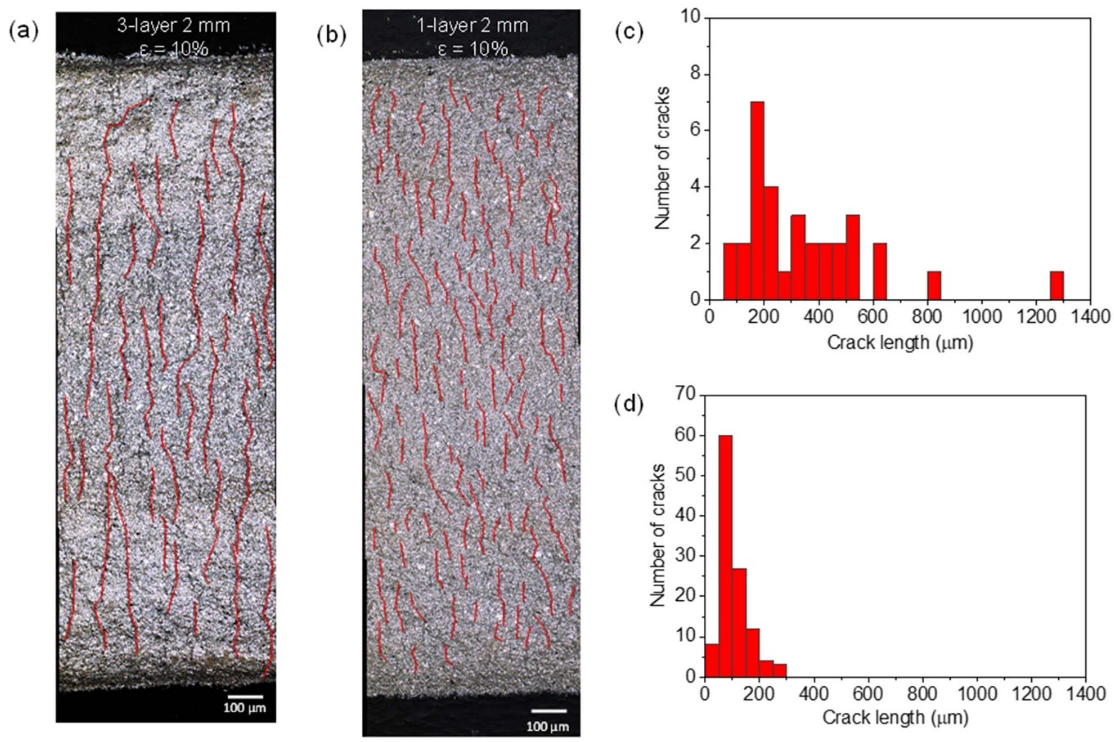

Figure 3. Crack patterns at $\varepsilon = 10\%$ with cracks highlighted for (a) 3-layer 2 and (b) 1-layer 2 mm specimens; distribution of crack lengths for shown crack patterns of (c) 3-layer and (d) 1-layer 2 mm specimens.

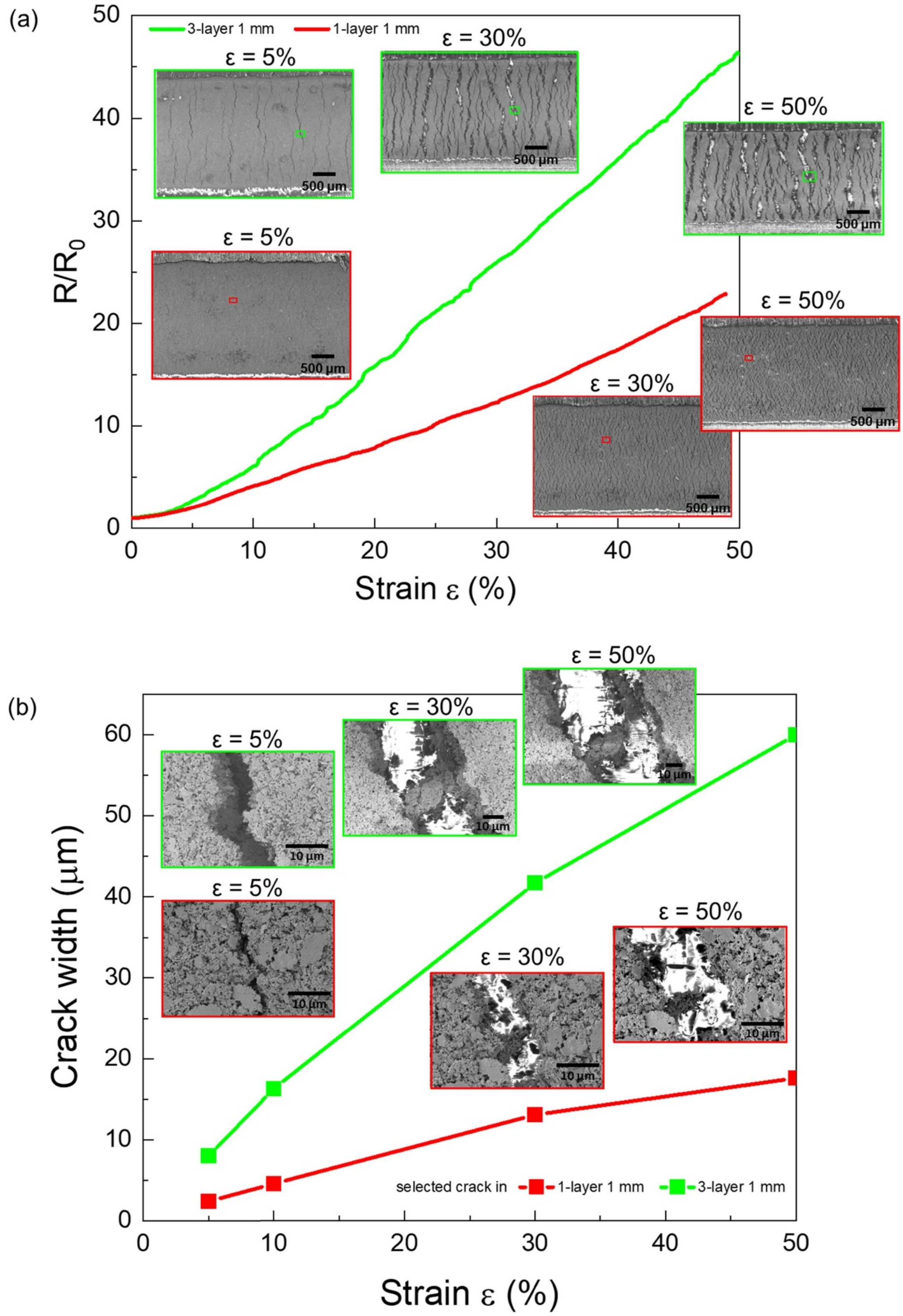

Figure 4. (a) Crack pattern images from *in-situ* SEM monotonic stretching tests with $R/R_0-\varepsilon$ evolution from corresponding *ex-situ* tests; (b) close-up images of representative cracks from *in-situ* SEM monotonic stretching tests with crack width–ε evolution.

long cracks even at 50% strain. Besides being longer, the cracks in the 3-layer ink are also notably wider (see figure 4(a)) the cracks in the 3-layer ink are also notably wider. Figure 4(b) shows higher magnification images of the crack width—ε evolution for selected cracks in the 3-layer and 1-layer specimens. The two selected cracks are representative of the widest, most well-developed cracks in the respective specimens. Both cracks were observed to widen and deepen simultaneously. The width of the crack in the 3-layer specimen was consistently 3–4 times the width of the crack in the 1-layer specimen up to an ε of

50%. Hence it is clear that crack widening, as well as deepening, is influenced by the ink thickness. For $\varepsilon = 30\%$, both of the selected cracks in figure 4(b) had clearly deepened to the ink-substrate interface and widened to more than 10 μm apart, with no contact between the silver flakes (whose sizes range from hundreds of nm to several μm) on the two crack faces. However, in both the 3-layer and 1-layer specimens, there were also some cracks and sections of cracks that did not appear to be wide enough to be through-thickness even at $\varepsilon = 50\%$.

Based on the above results, it can be seen that the different $R/R_0 - \varepsilon$ evolution behaviors for varying ink thickness correlate strongly with the corresponding differences in the crack pattern. The impact of ink thickness on the crack pattern at a given ε can be understood by the following fracture mechanics relation between the energy release rate $\mathcal{G}$ of a crack in a thin film and the film thickness h [53, 54].

$$\mathcal{G} = \left(\frac{\sigma_0^2 h}{\bar{E}_f}\right) Z. \tag{4}$$

The energy release rate $\mathcal{G}$ is proportional to the film thickness h. The proportionality is determined by the stress σ_0 on the crack faces, the plane strain elastic modulus $\bar{E}_f = E_f / \left(1 - \nu_f^2\right)$ of the film where E_f and ν_f are respectively the ink elastic modulus and Poisson's ratio, and the dimensionless number Z depending on the Dundur's parameters α and β as well as dimension ratios including the ratio H/h between the substrate thickness H and ink layer thickness h. Hence the driving force for crack extension in the 3-layer ink is expected to be roughly three times that of the 1-layer ink. In addition, the dependence of Z on H/h means that $\mathcal{G}$ is greater for a larger h given the same H, especially for $H/h < 10$ [55]. For the 1-layer and 3-layer ink specimens, the H/h ratio is about 13 and 5 respectively. This difference is expected to increase the $\mathcal{G}$ of the 3-layer ink to slightly more than three times that of the 1-layer ink.

The greater driving force for crack extension for the thicker ink corroborates with the observed longer cracks in the 3-layer ink compared to the 1-layer ink. The effect of the crack pattern on electrical resistance was investigated by Glushko *et al* [56] for metallic films on polymer substrates. From finite element modeling results, the normalized resistance was found to increase with the fourth order of crack length and second order of area crack density. Using their relationship and the average crack length and area crack density found in figure 3, the R/R_0 was calculated to be 2.2 for the 1-layer and 8.5 for the 3-layer 2 mm specimen at an ε of 10%. The corresponding average R/R_0 from the experiments were 3.68 ± 0.35 and 6.88 ± 0.47, respectively. The predicted R/R_0 are not too far off, highlighting the significant effect of the crack pattern, especially the crack length, on resistance evolution. However, the model by Glushko *et al* assumes through-thickness cracks that are perfectly insulating, a reasonable assumption for metallic (i.e. stiff) thin films on compliant polymer substrates. In the case of the PE874 conductive ink, not all cracks are through-thickness, especially at lower applied strains, as was shown in figure 4. Given that the same silver flakes (with sizes ranging from several μm to hundreds of nm) were used in the 1-layer and 3-layer ink, the greater width of the cracks in the 3-layer ink meant that a smaller portion of the total crack face area would be bridged by the silver flakes compared to the 1-layer ink at the same level of ε. Therefore the widening and deepening of the cracks could be a secondary mechanism causing the difference in $R/R_0 - \varepsilon$ evolution with varying ink thickness, other than the crack length dependence on ink thickness.

The longer cracks associated with thicker ink, resulting from the greater driving force for crack extension, play a key role in the more drastic trace width effect seen with the 3-layer ink compared to the 1-layer ink. The longer cracks in the 3-layer ink were able to traverse a 0.5 mm trace line at about 10% strain, leading to more drastic crack widening at higher strains and therefore more increase in R/R_0. The shorter cracks in the 1-layer ink could not traverse the 0.5 mm trace line even at high strains (>50%), hence the less drastic increase in R/R_0 (figure S1 in supporting information).

3.2. Cyclic behavior

Uniaxial cyclic stretching (fatigue) experiments were used to study the effect of repeated deformation on the conductive ink. Figure 5(a) shows the R/R_0 evolution with cyclic tensile stretching for three fatigue tests with a mean strain ε_m of 30% and different strain amplitudes ε_a of 12%, 15%, and 18%. The electrical resistance of the ink cycles between a maximum and minimum during every loading cycle. The maximum R/R_0 during the loading cycle steadily increases as the number of cycles increase. Eventually, a point of instability is reached where R/R_0 no longer increases steadily but instead experiences irregular jumps of increase with further cycling. In figure 5(a), the onset of instability is marked by the colored arrows. For these three tests, the onset of instability occurred at a high R/R_0 of 800 or above. Figure S2 in the supporting information shows the R/R_0 at the onset of instability plotted against the number of cycles to instability $N_{\text{instability}}$ for all fatigue tests excluding the *in-situ* ones. For most of the tests, the onset of instability occurred at a R/R_0 higher than 100. Therefore, we define the fatigue life N_f by the number of cycles until a R/R_0 of 100 is reached. In a previous work by Cahn *et al* [47], fatigue life was instead defined by the number of cycles until a R/R_0 of 500 is reached.

Figure 5(b) shows the R/R_0 maxima per cycle for the three forementioned tests as well as the rate of change in R/R_0 with respect to cycles $N - \mathrm{d}(R/R_0)/\mathrm{d}N$ or $(R/R_0)'$ for shorthand. A value of $(R/R_0)' = 1$

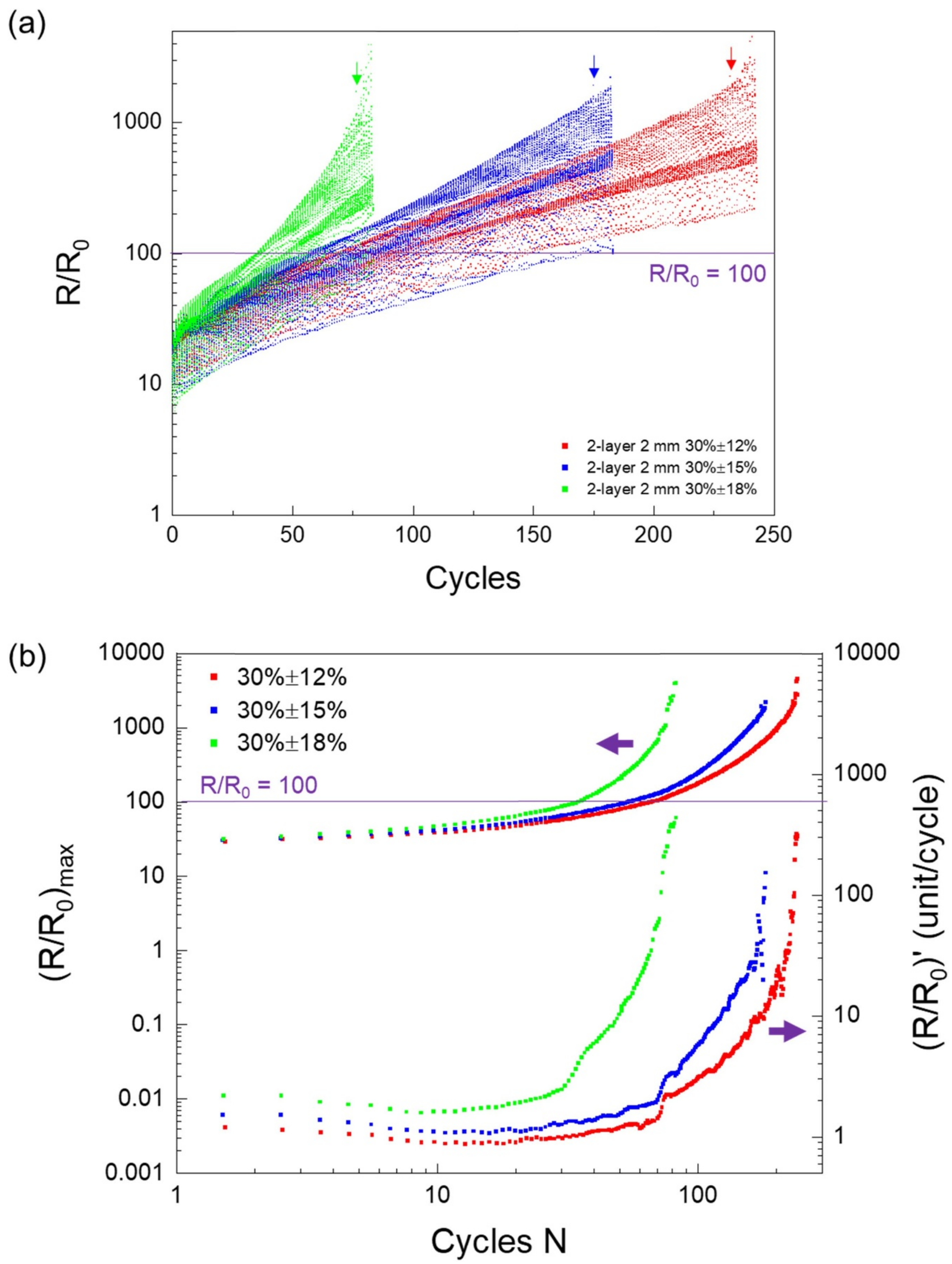

Figure 5. (a) R/R_0 evolution over cycles for the 2-layer 2 mm tests at strains 30% ± 12%, 30% ± 15%, and 30% ± 18%; (b) R/R_0 maxima over cycles and rate of change in normalized resistance with cycles $(R/R_0)'$ for forementioned tests.

means that R/R_0 increases by 1 every cycle. The rate $(R/R_0)'$ is found to always decrease during the initial portion of the fatigue test, and is therefore at a local maximum on cycle 1. For the tests with a large strain amplitude ($\varepsilon_a > 10\%$), as illustrated in figure 5(b), $(R/R_0)'$ decreases to a minimum within the first 20–30 cycles, and then increases steadily until the onset of instability. The normalized resistance R/R_0 has not reached 100 when the rate reaches its minimum. However, once the rates have significantly increased (i.e. $(R/R_0)' > 5$ or 10), R/R_0 has well exceeded 100: for practical purposes, the ink is not functional anymore at that stage. For tests with a small strain amplitude ($\varepsilon_a \leqslant 5\%$), $(R/R_0)'$ does not see any increase with cycling, but instead sees a phase of slower decrease or plateauing until the onset of instability (see figure S3 in the supporting information showing an example of the $(R/R_0)'$ evolution for $\varepsilon_a = 1\%$). Hence, the initial rate of resistance increase, $(R/R_0)'_i$, is a relevant parameter, which for example could be used to predict resistance evolution in a conservative manner, given that it is a local maximum.

Figure 6(a) shows the initial (local maximum) and the minimum $(R/R_0)'$ for all tests in the current work, plotted against the strain amplitude ε_a. Both $(R/R_0)'_i$ and $(R/R_0)'_{min}$ showed a strong correlation with ε_a, as highlighted by the blue trend lines in figure 6(a). Results from the tests with the 2-layer 2 mm-wide specimens show that between strain amplitudes of 1% and 18%, $(R/R_0)'_i$ increased by about 2 orders of magnitude from 0.032 to 3.22. The difference between $(R/R_0)'_i$ and $(R/R_0)'_{min}$ as indicated by the blue envelope was much greater at the ε_a of 1% (more than an order of magnitude) than at the ε_a of 18% (about only 2–3 times). The effect of the mean strain ε_m on $(R/R_0)'$ appears to be much less significant, based on the two specimens tested at $\varepsilon_a = 2\%$ having similar rates despite having different ε_m (15% vs 60%). Trace width appears to have a significant effect on $(R/R_0)'$, with the 0.5 mm-wide specimens generally having a higher $(R/R_0)'_i$ and $(R/R_0)'_{min}$ than the 2 mm-wide specimens.

Figure 6(b) shows $(R/R_0)'_i$ plotted against the number of ink layers for the 65% ± 15%, 10% ± 10%, and 15% ± 5% tests. The $(R/R_0)'_i$ increased with ink thickness, especially for the 65% ± 15% and 10% ± 10% cases. For practical purposes, however, the rate of change in resistance R with cycles dR/dN (or R' for shorthand) is the more useful parameter than $(R/R_0)'$ in characterizing resistance increase across different ink geometric dimensions. Figure 6(b) also shows that R'_i decreased with ink thickness, which corresponds to a slower increase in R with cycling and a longer fatigue life. Therefore, thicker ink layers are beneficial to maintaining a low resistance after repeated deformation.

Figure 7 shows the strain amplitude ε_a—fatigue life N_f curve, for all tests with 2-layer 2 mm-wide specimens. The measured N_f ranges from 36 cycles for the 30% ± 18% test to over 100 000 cycles (run-out test) for the 15% ± 1% test. There exists a strong correlation between measured N_f and ε_a, which was fitted to a power law function in that figure. Other than ε_a, the mean strain ε_m also affects N_f. For example, N_f was 86 533 cycles for the 15% ± 2% test, but only 57 572 cycles for the 60% ± 2% test. The ε_m effect on N_f is likely mainly due to its effect on R/R_0 at the maximum applied strain (equaling $\varepsilon_m + \varepsilon_a$) during the first cycle. However, ε_a has a more significant effect on N_f than ε_m. The relative importance of ε_a and ε_m in determining N_f is highlighted by comparing the 60% ± 2% test ($N_f = 57\,572$ cycles) with the 15% ± 5% tests ($N_f < 800$ cycles).

To better understand the ink deformation mechanisms responsible for the resistance increase with cyclic stretching, *in-situ* confocal microscope and SEM fatigue experiments were performed for this work.

The *in-situ* confocal microscopy fatigue experiment was performed at lower strains than in [47] to examine the evolution of the ink surface topography, particularly the surface cracks, during cycling. A 3-layer 2 mm-wide specimen was cycled at 10% ± 10% strain for 400 cycles under the optical and laser confocal microscope. Figures 8(a), (c) and (f) show the optical images at the maximum strain during cycle 1, 100, and 400; figure 8(b) shows the R/R_0 evolution over the cycles. The fatigue life N_f was reached at 118 cycles, which is very close to the N_f of 121 measured in the *ex-situ* test. This *in-situ* confocal microscope experiment differed from the 65% ± 15% strain experiment with the 1-layer 0.5 mm-wide specimen performed by Cahn *et al* [47] in that the 3-layer 2 mm-wide specimen was cycled at much lower strains, which should facilitate the examination of crack deepening with cycling since many of the cracks should not be through-thickness on cycle 1.

Superposing the laser profilometry scans of the same area taken during cycles 1 and 100 (or 400) at maximum strain, a height delta map between cycles 1 and 100 (or 400) can be generated by subtracting the ink height profile data for the two cycles pixel by pixel. The exact alignment of the laser profilometry data from the two cycles is performed with the aid of DIC in order to remove the small shifts in displacement between the two scans. A detailed explanation for the alignment process can be found in Cahn *et al* [47]. Figures 8(d) and (g) show the height delta maps between cycles 1 and 150 and between cycles 1 and 400, respectively. Figures 8(e) and (h) show line scans over the height delta maps for cycles 1–100 and for cycles 1–400 along the red lines marked in figures 8(d) and (e). For both the cycles 1–100 and cycles 1–400 height delta maps, a significant portion of the crack pattern had deepened with respect to their surrounding regions after cycling, though the in-plane crack pattern has remained the same. Based on the differences in the height delta data between cracks 1–4 and their surrounding regions in the line scans, the crack deepening occurred by an average of 10 μm between cycles 1 and 100 and 13 μm between cycles 1 and 400. Comparing the height delta maps and line scans for cycles 1–100 and cycles 1–400, some of the crack openings, most notably crack 3 and 4, also appeared to have widened while they deepened with cycling.

To obtain conclusive evidence of crack widening with cycling, a *in-situ* SEM experiment was performed to cyclically stretch a 3-layer 1 mm-wide specimen at strains of 30% ± 20%, after first monotonically stretching the specimen to an applied strain of 50% as a part of the first cycle (figure 3). Figure 9(p) shows the first 10 cycles of the R/R_0 evolution from a separate *ex-situ* test; the SEM *in-situ* test was expected to have the same R/R_0 evolution, with R/R_0 reaching

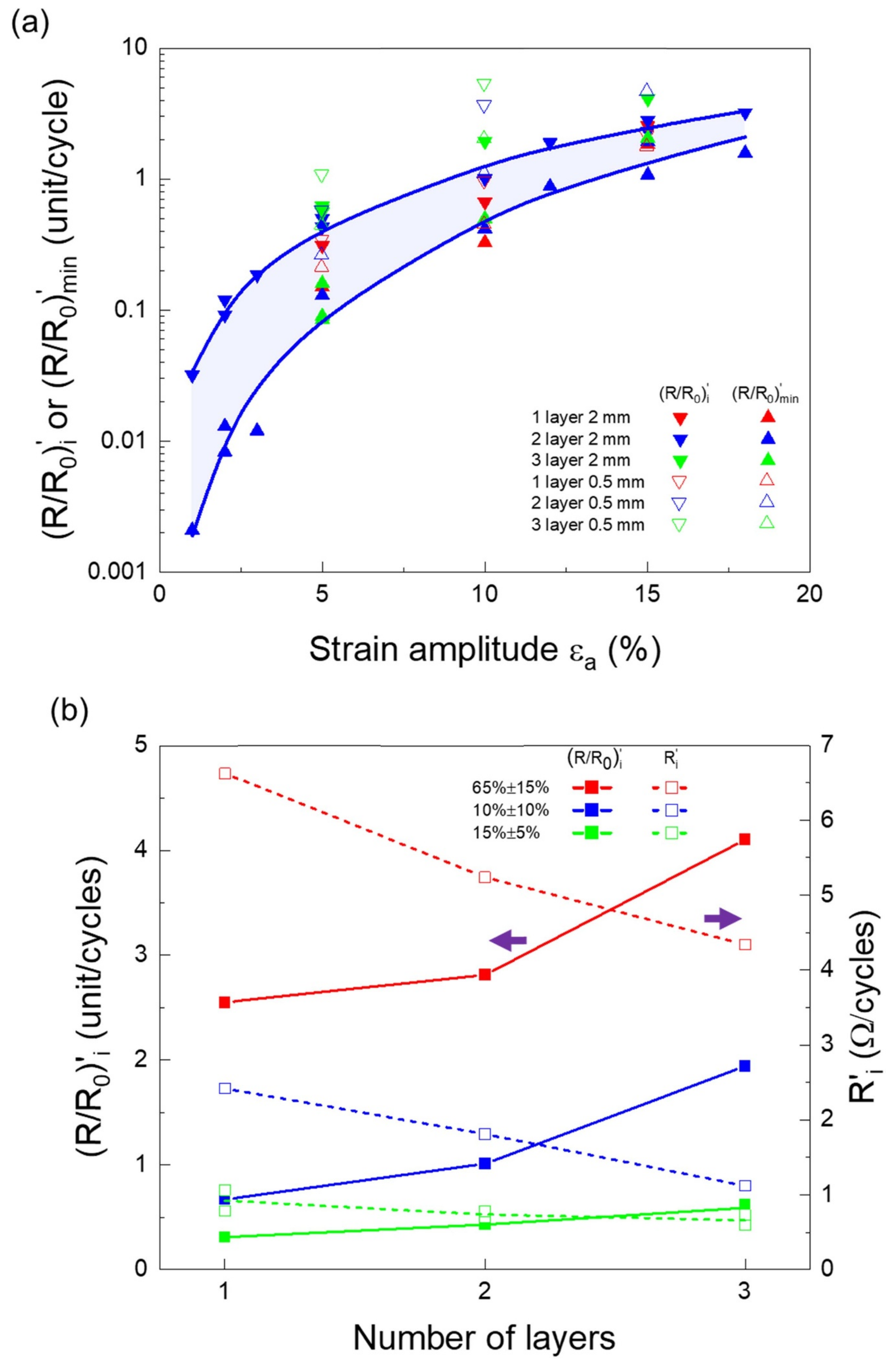

Figure 6. (a) $(R/R_0)'_{\mathrm{i}}$ and $(R/R_0)'_{\mathrm{min}}$ versus strain amplitude; (b) number of ink layers versus $(R/R_0)'_{\mathrm{i}}$ and R'_{i}.

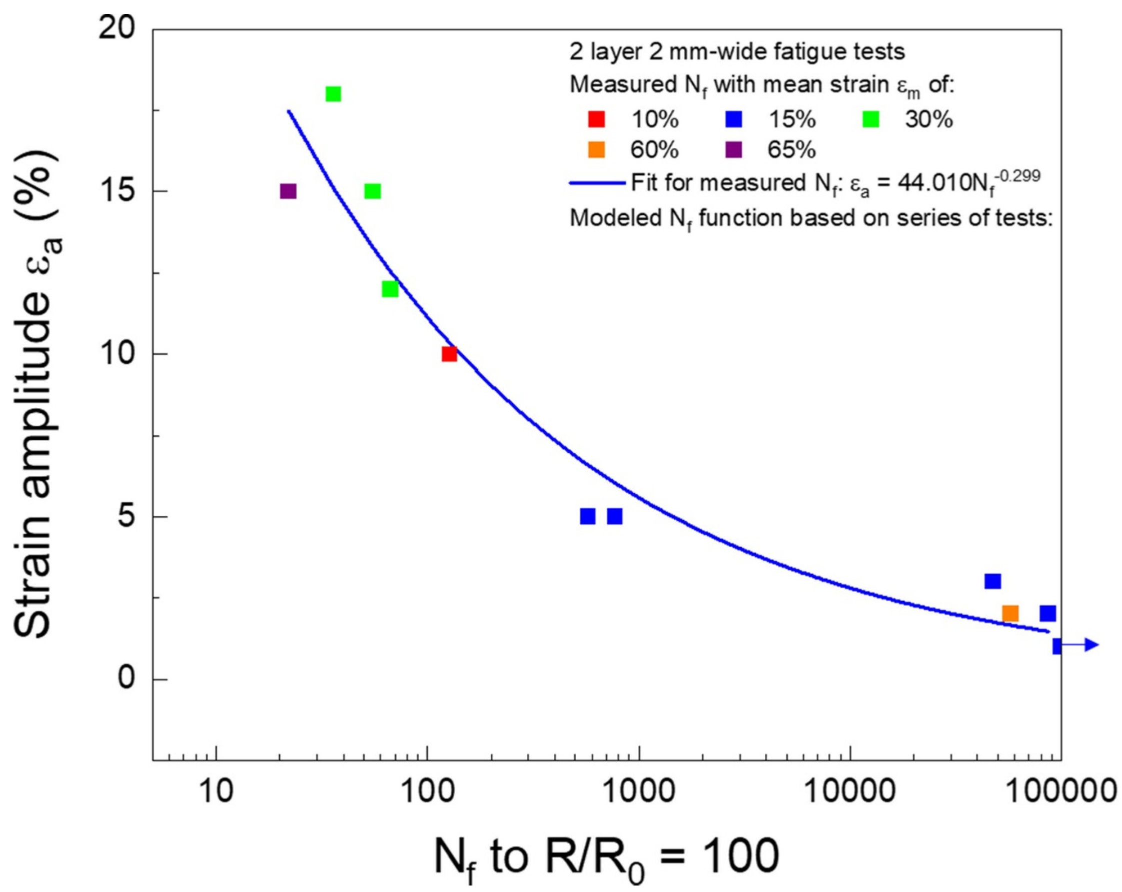

Figure 7. Strain amplitude versus measured fatigue life N_f.

about 90 at cycle 10. Figures 9(a)–(e) show the crack pattern at 50% strain during cycles 1, 2, 3, 5, and 10 for a 1.75 mm long section of the trace line roughly centered at the midpoint between the grips of the testing stage. While the extent of the crack pattern appears to remain unchanged over the cycles at low magnification, higher magnification images of the cracks showed clear evidence of their widening with cycling.

Figures 9(f)–(j) show close-up images of the widening of a representative narrow crack over the cycles. On cycle 1, the width of the crack measured about 1.6 μm at the point marked in figure 9(f). From cycle 1 to cycle 5, the width of the crack increased to about 6.4 μm. On cycle 1, the two cracks faces were very close to each other and the silver flakes could be seen to bridge the crack. By cycle 5, the crack faces were completely separated from each other and the silver flakes could no longer bridge the crack, likely resulting in a complete loss of electrical conductivity across that crack. Figures 9(k)–(o) show close-up images of the widening of a representative wide crack with an island of ink forming a linkage in the crack opening. From cycle 1 to cycle 2, the crack widened by about 3 μm on the left side. In the subsequent cycles, parts of the ink island were observed to shift and break off in a direction transverse to loading, causing damage the ink linkage across the crack opening. The evolution of the ink linkage observed in figures 9(k)–(o) shows how fatigue damage could sever an otherwise conductive path across a wide crack opening. At higher applied strains (>30%), many of the apparently coalesced cracks were still separated at junctions by ink linkages that could provide conductive pathways. Fatigue damage to these ink linkages by crack widening likely represents a significant mechanism for reducing the electrical conductivity.

Figures 9(q)–(t) show the in-plane tensile strain maps (Exx) for the crack patterns at cycles 2, 3, 5, and 10 shown in figures 9(b)–(e). The strain maps used the image at 50% strain during cycle 1 (figure 9(a)) as the reference image and the images at 50% strain during cycles 2, 3, 5, and 10 (figures 9(b)–(e)) as the current images to obtain the tensile strain changes generated during cycling. The crack widening, as shown by the positive strain distributions, were concentrated in the already formed cracks near the midpoint between the grips on cycle 2. During the subsequent cycles, the cracks further away from the midpoint began to widen more, as can be seen in the progression of the strain maps for cycles 3–10. As some

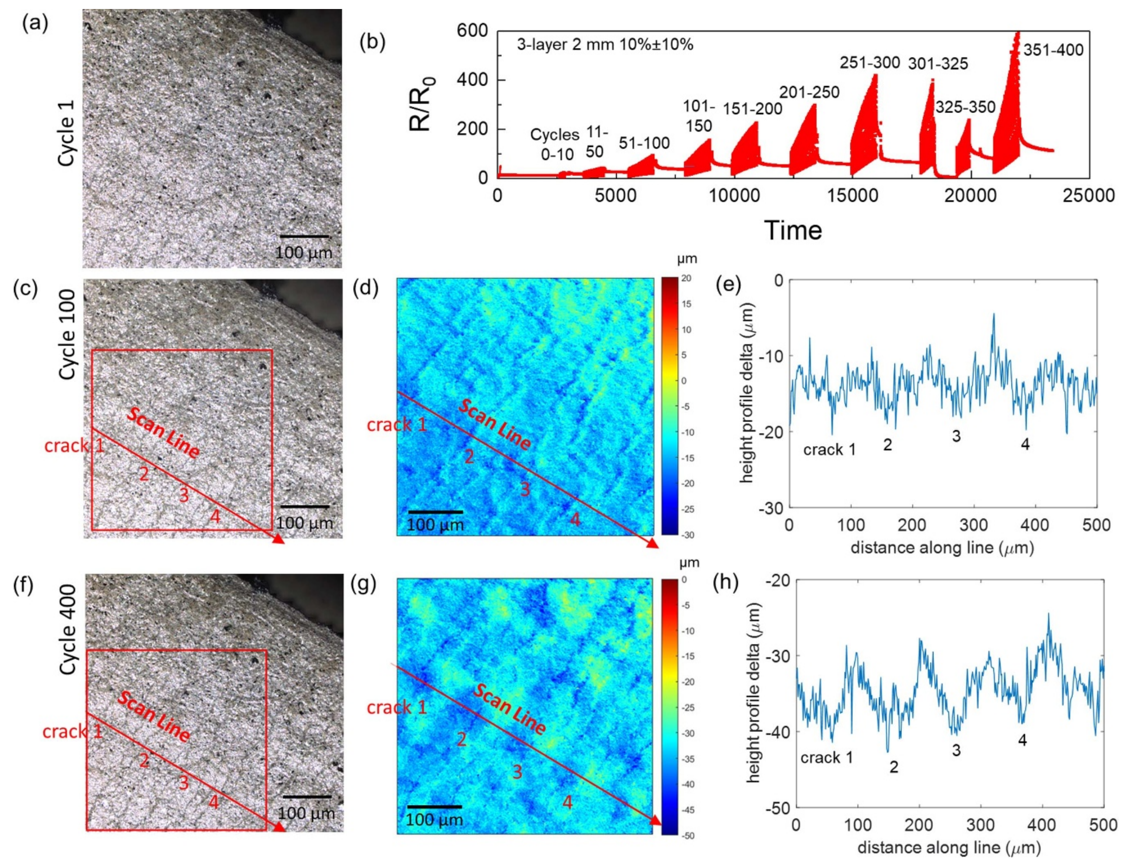

Figure 8. (a) Optical image at maximum strain on cycle 1 from *in-situ* confocal microscope cyclic stretching test; (b) R/R_0 evolution over cycles; (c) optical image at maximum strain on cycle 100; height profile delta map (d) and height profile delta line scan (e) between cycles 1 and 100; (f) optical image at maximum strain on cycle 400; height profile delta map (g) and height profile delta line scan (h) between cycles 1 and 400.

cracks widened, other cracks were compressed and narrowed, resulting in the negative strain distribution over them. In the area analyzed by the DIC strain maps, the ratio of the number of widening cracks to the number of narrowing cracks was about 2–1.

3.3. Degradation mechanisms

The results of the *in-situ* SEM experiments, from both the monotonic and cyclic parts, showed that the basic mode of microstructure damage in the ink is the simultaneous widening and deepening of the cracks. One notable distinction in damage mechanism between monotonic strain increase and cycling between two strain values is that the crack length increased significantly during the former (i.e. with increasing applied strain) but remained unchanged during the latter (i.e. with increasing numbers of cycles). This key difference is illustrated in the schematics of figure 10 showing the damage mechanisms for the monotonic and cyclic scenarios, with the top and cross-section views for the ink layer mounted on the substrate.

Knowing the difference in damage mechanism between the monotonic strain increase and cycling between two strain values, the electrical resistance increase during cyclic stretching to the same strain must therefore be entirely attributed to crack widening and deepening, whereas, as shown earlier, the lengthening of the cracks is a major contributor to resistance increase with increasing applied strain. The fact that the cracks do not lengthen with cycling means that the associated range in strain energy release rate, $\Delta\mathcal{G}$, is not large enough for fatigue-driven crack extension in the polyurethane binder of the ink. Instead, the widening of the cracks under cyclic loading is likely a result of unlocking of adjacent silver flakes during the repeated back-and forth motion of the crack faces. Another possible fatigue mechanism for crack widening is the fatigue of the TPU substrate at the location of the cracks once they reach the interface, as suggested by a post-mortem (unloaded specimen) FIB cross section of a fatigued specimen (see red arrows in figure S4 in the supporting information). This understanding of the fatigue damage mechanism in a conductive ink is in agreement with the observed relation between fatigue resistance increase and through-thickness cracking for a polymer-supported metal thin film found by Gebhart *et al* [57].

The delamination between the film and substrate, often found in thin metal films supported by polymer

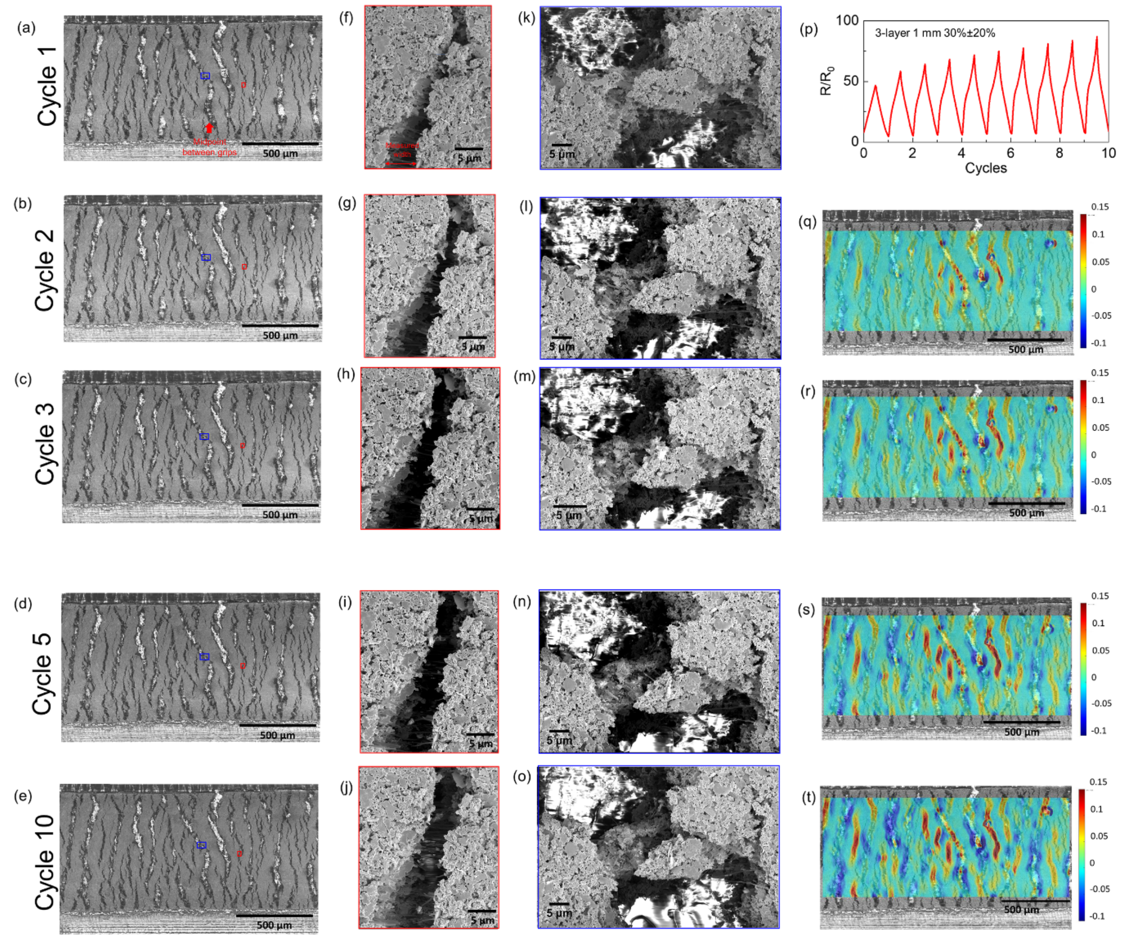

Figure 9. (a)–(e) Crack pattern images for cycles 1, 2, 3, 5, and 10 of *in-situ* SEM cyclic stretching test; closeup images of representative narrow crack (f)–(j) and wide crack with ink linkage (k)–(o) over the cycles; (p) R/R_0 evolution over cycles from corresponding *ex-situ* test; (q)–(t) DIC strain maps for cycles 2, 3, 5, and 10. The sample is uniaxially stretched along the horizontal direction of the images.The corresponding strain maps show the in-plane Exx component.

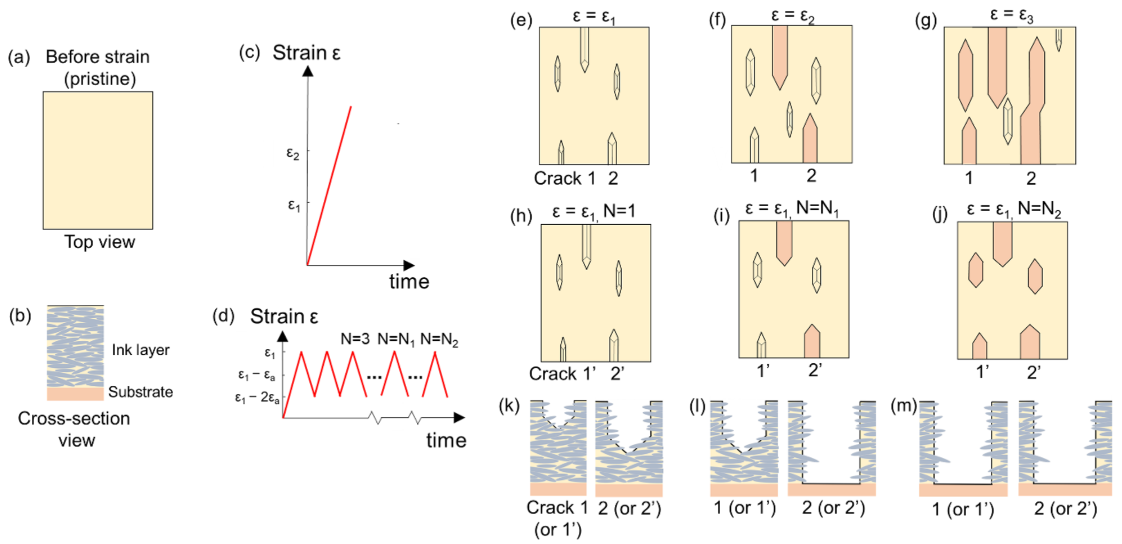

Figure 10. Schematic diagrams showing the top view (a) and cross-section view (b) of the ink layer; the monotonic (c) and cyclic (d) straining scenarios; top view of the ink layer surface during monotonic (e)–(g) and cyclic (h)–(j) straining; cross-section view of the ink layer during monotonic and cyclic straining (k)–(m).

substrates [50, 58], was not observed for the conductive ink under tensile strain. Therefore the adhesion between the ink layer and substrate can generally be assumed to be good. However, microstructural voids located at the ink-substrate interface could represent an important factor contributing to the initiation of cracking in the ink layer. The role of these voids in crack initiation awaits further investigation by *in-situ* SEM experiments with ink layer cross-sectioning.

This work showed that ink thickness and trace width impact the electrical resistance evolution with tensile strain under monotonic and cyclic loading, due to differences in crack pattern resulting from stretching. For practical applications, thicker ($\geqslant$25 μm) and wider ($\geqslant$2 mm) inks should be used to lower R increases with repeated deformation. The interconnects in devices have optimized configurations such as the serpentine, whereby the local strains can be one order of magnitude lower than the applied strain [44, 46]. Therefore, the strain amplitudes involved in the repeated straining of serpentine interconnects are likely to be small (<5%), which means that the PE874 ink can withstand large numbers of cycles (>1,000) in stretchable applications. The knowledge and characterization of resistance evolution of the ink cycled at small strain amplitudes, gained from this work using straight trace line specimens (and uniform strain distributions), will be used in a future work to model the resistance evolution and fatigue life of serpentine interconnects.

4. Conclusions

The current work examined the electrical response of the stretchable PE874 conductive ink to uniaxial monotonic and cyclic stretching for different ink geometry (1, 2, and 3 layers, each layer approximately 8–10 μm, and trace widths of 0.5, 1, and 2 mm) and loading conditions. The material deformation mechanisms responsible for the electrical resistance evolution with monotonic tensile strain and cyclic straining were also investigated. Based on the experimental results, including those of the *in-situ* confocal microscope and SEM experiments, the following conclusions can be drawn.

(a) Ink geometric conditions, including both ink thickness and trace width, impact the electrical resistance evolution with tensile strain, due to differences in crack pattern resulting from stretching. Narrow trace widths (0.5 mm) are associated with much higher resistance, as cracks traverse the trace width. Thicker inks are associated with higher normalized resistance, in part due to longer cracks. However, when taking into account the thickness effect on initial resistance, thicker inks provide slightly better resistance under strain.

(b) For cyclic stretching, there exists a strong correlation between fatigue life N_f, as defined by the number of cycles until a R/R_0 of 100 is reached, and the strain amplitude ε_a. The mean strain ε_m has a secondary effect on N_f.

(c) The initial normalized resistance rate $(R/R_0)'_i$ is found to scale with ε_a. Therefore this parameter can likely be used to conservatively predict resistance increase for a cyclic test.

(d) The rate of change in resistance R with cycling, dR/dN (or R'), decreases with ink thickness and trace width for fatigue tests across different strain levels. For practical applications, thicker ($\geqslant$25 μm) and wider ($\geqslant$2 mm) inks should be used to lower R increases with repeated deformation.

(e) During monotonic tensile strain increase, the cracks lengthened as well as widened and deepened; during cyclic stretching between two strain values, the cracks did not lengthen noticeably but still widened and deepened. Fatigue damage from crack widening and deepening was found to be responsible for electrical resistance increase during cyclic stretching to the same strain. The loss of electrical conductivity could be considered to occur when the crack has effectively deepened to the ink-substrate surface as the crack faces become completely separated and become much wider than the largest flake in the ink.

Data availability statement

The data that support the findings of this study are available upon reasonable request from the authors.

Acknowledgments

The authors gratefully acknowledge funding support from the National Science Foundation (NSF CMMI-MOMS: 2026936). The authors are grateful to DuPont colleagues (Jeff Meth, Lynne Dellis and Augustus Jones) for providing samples.

ORCID iDs

A Antoniou https://orcid.org/0000-0002-5270-5438
O Pierron https://orcid.org/0000-0003-0787-7457

References

[1] Gao W *et al* 2016 Fully integrated wearable sensor arrays for multiplexed *in situ* perspiration analysis *Nature* **529** 509–14
[2] Imani S, Bandodkar A J, Mohan A M V, Kumar R, Yu S, Wang J and Mercier P P 2016 A wearable chemical–electrophysiological hybrid biosensing system for real-time health and fitness monitoring *Nat. Commun.* **7** 1–7

[3] Lee H *et al* 2016 A graphene-based electrochemical device with thermoresponsive microneedles for diabetes monitoring and therapy *Nat. Nanotechnol.* **11** 566–72
[4] Schwartz G, Tee B C-K, Mei J, Appleton A L, Kim D H, Wang H and Bao Z 2013 Flexible polymer transistors with high pressure sensitivity for application in electronic skin and health monitoring *Nat. Commun.* **4** 1–8
[5] Huang X, Liu Y, Zhou J, Nejad S K, Wong T H, Huang Y, Li H, Yiu C K, Park W and Li J 2022 Garment embedded sweat-activated batteries in wearable electronics for continuous sweat monitoring *Npj Flex. Electron.* **6** 1–8
[6] Iqbal S, Mahgoub I, Du E, Leavitt M A and Asghar W 2021 Advances in healthcare wearable devices *NPJ Flex. Electron.* **5** 1–14
[7] Dubal D P, Chodankar N R, Kim D-H and Gomez-Romero P 2018 Towards flexible solid-state supercapacitors for smart and wearable electronics *Chem. Soc. Rev.* **47** 2065–129
[8] Lv T, Liu M, Zhu D, Gan L and Chen T 2018 Nanocarbon-based materials for flexible all-solid-state supercapacitors *Adv. Mater.* **30** 1–17
[9] García Núñez C, Manjakkal L and Dahiya R 2019 Energy autonomous electronic skin *Npj Flex. Electron.* **3** 1–24
[10] Gupta S, Navaraj W T, Lorenzelli L and Dahiya R 2018 Ultra-thin chips for high-performance flexible electronics *Npj Flex. Electron.* **2** 1–17
[11] Kim S *et al* 2011 Low-power flexible organic light-emitting diode display device *Adv. Mater.* **23** 3511–6
[12] Rogers J A *et al* 2001 Paper-like electronic displays: large-area rubber-stamped plastic sheets of electronics and microencapsulated electrophoretic inks *Proc. Natl Acad. Sci.* **98** 4835–40
[13] Sekitani T, Nakajima H, Maeda H, Fukushima T, Aida T, Hata K and Someya T 2009 Stretchable active-matrix organic light-emitting diode display using printable elastic conductors *Nat. Mater.* **8** 494–9
[14] Park Y, Fuentes-Hernandez C, Kim K, Chou W-F, Larrain F A, Graham S, Pierron O N and Kippelen B 2021 Skin-like low-noise elastomeric organic photodiodes. *Sci. Adv.* **7** eabj6565
[15] Chen Y, Zhang Y, Liang Z, Cao Y, Han Z and Feng X 2020 Flexible inorganic bioelectronics *Npj Flex. Electron.* **4** 1–20
[16] Choi M K, Yang J, Hyeon T and Kim D-H 2018 Flexible quantum dot light-emitting diodes for next-generation displays *Npj Flex. Electron.* **2** 1–14
[17] Kim S H, Song S Y, Kim S Y, Chang M W, Kwon H J, Yoon K H, Sung W Y, Sung M M and Chu H Y 2022 A compact polymer–inorganic hybrid gas barrier nanolayer for flexible organic light-emitting diode displays *Npj Flex. Electron.* **6** 1–6
[18] Hong Y J, Jeong H, Cho K W, Lu N and Kim D-H 2019 Wearable and implantable devices for cardiovascular healthcare: from monitoring to therapy based on flexible and stretchable electronics *Adv. Funct. Mater.* **29** 1–26
[19] KIm D *et al* 2011 Materials for multifunctional balloon catheters with capabilities in cardiac electrophysiological mapping and ablation therapy *Nat. Mater.* **10** 316–23
[20] Chow J H, Sitaraman S K, May C and May J 2018 Study of wearables with embedded electronics through experiments and simulations *2018 IEEE 68th Electronic Components and Technology Conf. (ECTC)* (IEEE) pp 814–21
[21] Yetisen A K, Martinez-Hurtado J L, Ünal B, Khademhosseini A and Butt H 2018 Wearables in medicine *Adv. Mater.* **30** 1706910
[22] Hommel M and Kraft O 2001 Deformation behavior of thin copper films on deformable substrates *Acta Mater.* **49** 3935–47
[23] Kraft O, Hommel M and Arzt E 2000 X-ray diffraction as a tool to study the mechanical behaviour of thin films *Mater. Sci. Eng.* **288** 209–16
[24] Lacour S P, Wagner S, Huang Z and Suo Z 2003 Stretchable gold conductors on elastomeric substrates *Appl. Phys. Lett.* **82** 2404–6
[25] Lambricht N, Pardoen T and Yunus S 2013 Giant stretchability of thin gold films on rough elastomeric substrates *Acta Mater.* **61** 540–7
[26] Niu R M, Liu G, Wang C, Zhang G, Ding X D and Sun J 2007 Thickness dependent critical strain in submicron Cu films adherent to polymer substrate *Appl. Phys. Lett.* **90** 16
[27] Xiang Y, Li T, Suo Z and Vlassak J J 2005 High ductility of a metal film adherent on a polymer substrate *Appl. Phys. Lett.* **87** 16
[28] Yu D Y and Spaepen F 2004 The yield strength of thin copper films on Kapton *J. Appl. Phys.* **95** 2991–7
[29] Cordill M J, Kreiml P and Mitterer C 2022 Materials engineering for flexible metallic thin film applications *Materials* **15** 926
[30] Kaiser T, Cordill M, Kirchlechner C and Menzel A 2021 Electrical and mechanical behaviour of metal thin films with deformation-induced cracks predicted by computational homogenisation *Int. J. Fract.* **231** 223–42
[31] Sim G-D, Lee Y-S, Lee S-B and Vlassak J J 2013 Effects of stretching and cycling on the fatigue behavior of polymer-supported Ag thin films *Mater. Sci. Eng.* A **575** 86–93
[32] Sim G-D, Hwangbo Y, Kim H-H, Lee S-B and Vlassak J J 2012 Fatigue of polymer-supported Ag thin films *Scr. Mater.* **66** 915–8
[33] Glushko O and Cordill M 2020 In-operando fatigue behavior of gold metallization lines on polyimide substrate *Scr. Mater.* **186** 48–51
[34] Cahn G, Barrios A, Graham S, Meth J, Antoniou A and Pierron O 2020 The role of strain localization on the electrical behavior of flexible and stretchable screen printed silver inks on polymer substrates *Materialia* **10** 100642
[35] Merilampi S, Laine-Ma T and Ruuskanen P 2009 The characterization of electrically conductive silver ink patterns on flexible substrates *Microelectron. Reliab.* **49** 782–90
[36] Shin D-Y, Lee Y and Kim C H 2009 Performance characterization of screen printed radio frequency identification antennas with silver nanopaste *Thin Solid Films* **517** 6112–8
[37] Kim S and Sung H J 2015 Effect of printing parameters on gravure patterning with conductive silver ink *J. Micromech. Microeng.* **25** 4
[38] Sung D, de la Fuente Vornbrock A and Subramanian V 2009 Scaling and optimization of gravure-printed silver nanoparticle lines for printed electronics *IEEE Trans. Compon. Packag. Technol.* **33** 105–14
[39] Borghetti M, Serpelloni M, Sardini E and Pandini S 2016 Mechanical behavior of strain sensors based on PEDOT: PSS and silver nanoparticles inks deposited on polymer substrate by inkjet printing *Sens. Actuators* A **243** 71–80
[40] Schlisske S, Raths S, Ruiz-Preciado L A, Lemmer U, Exner K and Hernandez-Sosa G 2021 Surface energy patterning for ink-independent process optimization of inkjet-printed electronics *Flex. Print. Electron.* **6** 015002
[41] Tafoya R R and Secor E B 2020 Understanding effects of printhead geometry in aerosol jet printing *Flex. Print. Electron.* **5** 035004
[42] van Osch T H, Perelaer J, De Laat A W and Schubert U S 2008 Inkjet printing of narrow conductive tracks on untreated polymeric substrates *Adv. Mater.* **20** 343–5
[43] Yang W, Mathies F, Unger E L, Hermerschmidt F and List-Kratochvil E J 2020 One-pot synthesis of a stable and cost-effective silver particle-free ink for inkjet-printed flexible electronics *J. Mater. Chem.* C **8** 16443–51
[44] Koshi T, Nomura K-I and Yoshida M 2021 Measurement and analysis on failure lifetime of serpentine interconnects for e-textiles under cyclic large deformation *Flex. Print. Electron.* **6** 025003
[45] Sliz R, Huttunen O-H, Jansson E, Kemppainen J, Schroderus J, Kurkinen M and Fabritius T 2020 Reliability of R2R-printed, flexible electrodes for e-clothing applications *Npj Flex. Electron.* **4** 1–9

[46] Zhang Y, Xu S, Fu H, Lee J, Su J, Hwang K-C, Rogers J A and Huang Y 2013 Buckling in serpentine microstructures and applications in elastomer-supported ultra-stretchable electronics with high areal coverage *Soft Matter* **9** 8062–70

[47] Cahn G, Pierron O and Antoniou A 2021 Electrical performance evolution and fatigue mechanisms of silver-filled polymer ink under uniaxial cyclic stretch *Flex. Print. Electron.* **6** 035008

[48] Cahn G, Pierron O and Antoniou A 2021 Trace width effects on electrical performance of screen-printed silver inks on elastomeric substrates under uniaxial stretch *J. Appl. Phys.* **130** 115304

[49] Blaber J, Adair B and Antoniou A 2015 Ncorr: open-source 2D digital image correlation matlab software *Exp. Mech.* **55** 1105–22

[50] Cordill M and Taylor A 2015 Thickness effect on the fracture and delamination of titanium films *Thin Solid Films* **589** 209–14

[51] Glushko O, Klug A, List-Kratochvil E J and Cordill M J 2017 Monotonic and cyclic mechanical reliability of metallization lines on polymer substrates *J. Mater. Res.* **32** 1760–9

[52] Taylor A A, Cordill M J and Dehm G 2012 On the limits of the interfacial yield model for fragmentation testing of brittle films on polymer substrates *Phil. Mag.* **92** 3363–80

[53] Hutchinson J W and Suo Z 1991 Mixed mode cracking in layered materials *Adv. Appl. Mech.* **29** 63–191

[54] Ye T, Suo Z and Evans A 1992 Thin film cracking and the roles of substrate and interface *Int. J. Solids Struct.* **29** 2639–48

[55] Vlassak J J 2003 Channel cracking in thin films on substrates of finite thickness *Int. J. Fract.* **119** 299–323

[56] Glushko O, Kraker P and Cordill M 2017 Explicit relationship between electrical and topological degradation of polymer-supported metal films subjected to mechanical loading *Appl. Phys. Lett.* **110** 191904

[57] Gebhart D D, Krapf A, Gammer C, Merle B and Cordill M J 2022 Linking through-thickness cracks in metallic thin films to *in-situ* electrical resistance peak broadening *Scr. Mater.* **212** 114550

[58] Cordill M J, Taylor A, Schalko J and Dehm G 2010 Fracture and delamination of chromium thin films on polymer substrates *Metall. Mater. Trans.* A **41** 870–5